# Strain response and energy dissipation of floating saline ice under cyclic compressive stress

Mingdong Wei[1], Arttu Polojärvi[1], David M. Cole[2], Malith Prasanna[1]

[1]Aalto University, School of Engineering, Department of Mechanical Engineering, P.O. Box 14100, FI-00076 Aalto, Finland.
[2]ERDC-CRREL (Ret.), 72 Lyme Rd., Hanover, NH 03768, USA

*Correspondence to*: Arttu Polojärvi (arttu.polojarvi@aalto.fi)

**Abstract.** Understanding the mechanical behavior of sea ice is the basis of ice mechanics applications. Laboratory-scale work on saline ice has often involved dry, isothermal ice specimens due to the relative ease of testing. This approach does not address the fact that the natural sea ice is practically always floating in seawater and typically has a significant temperature gradient. To address this important issue, we have developed equipment and methods for conducting compressive loading experiments on floating laboratory-prepared saline ice specimens. The present effort describes these developments and presents the results of stress-controlled sinusoidal cyclic compression experiments. We conducted the experiments on dry, isothermal (-10°C) ice specimens and on floating ice specimens with a naturally occurring temperature gradient. The experiments involved ice salinities of 5 and 7 ppt, cyclic stress levels ranging from 0.04–0.12 MPa to 0.08–0.25 MPa and cyclic loading frequencies of 0.001 Hz to 1 Hz. The constitutive response and energy dissipation under cyclic loading were successfully analyzed using an existing physically based constitutive model for sea ice. The results highlight the importance of testing warm and floating ice specimens and demonstrate that the experimental method proposed in this study provides a convenient and practical approach to perform laboratory experiments on floating ice.

## 1 Introduction

Climate change has led to an increased interest in polar sea areas and on ice behavior, since accurate predictions on the evolution of the ice conditions are crucial for modeling the future climate. Warming climate has also resulted in a search for more efficient marine transit routes, production of offshore wind power, industrial operations related to extraction of hydrocarbons, and even tourism in the north (Gagne et al., 2015; Serreze and Stroeve, 2015; Kern et al., 2019). Structural loads due to sea ice make these activities challenging. In-depth understanding of the physical and mechanical properties of sea ice is required to develop tools for modeling future ice conditions, the related ice–ice and ice–wave interaction problems, and for the design of safe and sustainable offshore structures

(Dempsey, 2000; Feltham, 2008, Herman et al., 2019a,b; Lu et al., 2018a,b; Ranta et al., 2017, 2018a,b; Tuhkuri

30    and Polojärvi, 2018; Polojärvi et al., 2015; Voermans et al., 2019; Cheng et al., 2019; Li et al., 2015).

This paper studies the mechanical behavior of laboratory-prepared saline ice specimens under cyclic loading. This type of loading occurs in wave–ice and some ice–ice and ice–structure interaction problems – all important in the changing polar environment. For example, warming climate causes an increase in the amount of open water and broken ice fields, which strengthens the impact of waves on sea ice. From the perspective of pure ice mechanics

35    and modeling of ice, the cyclic loading experiments yield information on the elastic and viscoelastic components of strain and their dependence on the physical, or microstructural, characteristics of the ice. The cyclic loading tests also give insight into the fatigue of ice (Haskell et al., 1996; Bond and Langhorne, 1997; Langhorne et al.,1998; Mellor and Cole, 1981; Murdza et al., 2019; Schulson and Paul, 2009; Iliescu et al., 2017; Iliescu and Schulson, 2002).

40    Cyclic loading experiments on freshwater ice have been performed since the forties (Kartashkin, 1947; Mellor and Cole, 1981) and on saline ice since the eighties (Tabata and Nohguchi, 1980; Cole, 1995; Cole and Durell, 1995; Cole et al., 1998). Cole and Durell (1995) studied the effects of temperature (from -5 to -50℃), cyclic stress amplitude (from 0.1 to 0.8 MPa) and loading frequency (from $10^{-3}$ to 1 Hz) on the response of laboratory-grown saline ice; the ice response was revealed sensitive to variations in these factors. Cole et al. (1998) investigated the

45    response of columnar first-year sea ice to cyclic loading and found that the elastic, anelastic, and viscous strains varied according to the relation between the loading and preferred c-axis directions of the specimens. More recently, Heijkoop et al. (2018) conducted strain-controlled cyclic compression tests on sea ice to ascertain the variation of storage and loss compliances versus frequency. All of this earlier work has been performed using isothermal, dry specimens.

50    An often-overlooked issue in laboratory-scale experimentation is that most sea ice problems involve ice that is floating on water. Floating ice commonly has a through-thickness temperature gradient, resulting in a through-thickness gradient in its mechanical properties. The latter point is important to address in experimentation and modeling. The temperature gradient is implicitly taken into account in in-situ experiments on floating ice (Langhorne et al., 2015; Smith et al., 2015; Wongpan et al., 2018). The cost of in-situ experimental campaigns,

55    however, is high and the experiments often require specially designed loading devices (Vincent and Dempsey, 1999; Dempsey et al., 1999, 2018; Cole and Dempsey, 2004). Consequently, the relatively low costs and convenience of laboratory-scale work motivate the development of viable methods for laboratory-scale experiments on floating ice. Such experiments can be used, for example, for thorough validation of material models aiming to account for the temperature gradient in ice.

60     In the study presented here, stress-controlled sinusoidal cyclic compression experiments were performed on laboratory-grown, non-oriented columnar saline ice specimens floating on salt water and repeated on dry, isothermal (-10°C) specimens. The varied parameters were the ice salinity, cyclic stress amplitude and mean stress level, and the frequency of cyclic loading. The results are comprehensively analyzed and discussed, and are shown to compare favorably with the predictions of an existing physically-based constitutive model (Cole,1995).

65     Techniques and observations yielding increased insight of the behavior of sea ice in its natural conditions are introduced; Insight on floating, rather warm, ice is important, as future sea ice is expected to be on average warmer than now (Boe et al., 2009; Blockley and Peterson, 2018; Ridley and Blockley, 2018).

    The paper is organized as follows. Section 2 describes the specimen preparation, the experimental set-up, and the matrix of experimental variables. Section 3 presents the results from the experiments. Section 4 addresses

70 constitutive modeling and Section 5 discusses our findings with references to earlier work and Section 6 gives our conclusions.

**2 Laboratory experiments of saline ice under cyclic loading**

**2.1 Saline ice specimen preparation and characterization**

    The ice was grown in the cold room of Department of Mechanical Engineering, Aalto University using a tank

75 having dimensions of 1.15 m × 1.15 m × 0.98 m (width × length × depth) and meltwater salinities of 24 and 34 ppt. Rigid foam insulation was placed on the sides and bottom of the tank and heating cables were placed around the bottom perimeter to inhibit freezing from the structural members of the tank. Additionally, a hose for draining excess water was installed near the base of the tank, to prevent the accumulation of water pressure under the ice sheet during its growth. Such pressure could cause microcracking of ice or generate additional loads on the tank.

80 Specimens having the nominal dimensions of 0.60 m × 0.30 m × 0.10 m were prepared by placing high-density polyethylene molds into the tank before seeding (Figure 1). The tolerance of the specimen dimensions was ±2 mm (in all stress calculations below, the measured dimensions of the specimens were used). The molds floated with 2–3 mm of freeboard. Next, the saline water was chilled to about -1.5°C, the cold room temperature dropped to ≈ -20°C and the tank was seeded by spraying very fine mist of fresh water over the tank as is typically done to seed

85 ice sheets in larger-scale test basins (Gow, 1984; Li and Riska, 1996).

    After the seeding, the room temperature was increased to -14°C for three days and then -10°C for two days to produce the desired specimen thickness of 10 cm. The ice sheets made using 24 ppt and 34 ppt-saline water reached average salinities of 5 and 7 ppt, respectively, and their densities were $886\pm19$ and $879\pm16$ kg·m$^{-3}$, respectively.

The specimens used in the dry experiments (Figure 2a and 3) were sealed in plastic bags and stored in a freezer at -10°C for 1–2 days before testing. However, for the floating ice experiments (see Figure 2b), the specimens were ejected from the molds, placed in plastic bags with water from the growth tank and quickly transferred to the test basin to minimize brine drainage during the transfer.

Before the experiments, the columnar microstructure of the ice was verified by producing and inspecting thin sections as detailed by Langway (1958). Of special interest was the microstructure close to the specimen boundaries since such molds are somewhat uncommon in ice specimen preparation. Figure 4 shows two typical thin sections from near the boundary of a specimen produced using 34-ppt-saline water; one is for the vertical and the other for the horizontal direction as indicated. Figure 4a shows the columnar structure of the ice. The horizontal view in Figure 4b provides a way to estimate the average grain size by dividing the section area by the number of grains; the average grain size was ≈ 3.5 mm. The Schmidt equal area net pole projection for one of the thin sections shown in Figure 5 confirms that the c-axes were unaligned in the horizontal plane, as intended.

### 2.2 Equipment, test matrix and experimental procedure

The experiments were conducted in the same cold chamber used for the saline ice production. As Figures 2 and 3 illustrate, an externally mounted electrohydraulic cylinder applied loads to the specimens. The piston passed through a sealed port in the side of the test tank. The piston had a maximum stroke of 800 mm and a loading capacity of 100 kN for compression and 60 kN for tension. The load cell had an accuracy of ± 5 N, which is sufficient for all stress levels and cycles of the experiments here. The test basin was constructed of waterproof plywood. The system employed a camera for remote monitoring of the experiments, a three-channel temperature datalogger to record the temperature profile of floating ice during testing, a Data Acquisition Processor (DAP) board (model: Data Translation DT9834), and fixtures for arranging displacement sensors to the ice specimens. The temperature datalogger had a maximum sampling rate of one datum per five seconds, its measurement range was from -100 to 1300°C, and an accuracy of ± 0.5°C. The DAP board could achieve a maximum scan rate of 500,000 samples per second.

The loading system has a self-equilibrating geometry in that the compressive force applied by the electrohydraulic piston and transmitted through the specimen is balanced by a tensile force in the external load frame (Figure 3). Care was taken to center the loading piston and the reaction plates on the vertical dimension of the load frame.

The ice deformation was measured as follows. Before the test, two holes were drilled on the specimen. Two iron rods with the cross-section of 5 mm × 5 mm were then inserted into the holes and frozen in place using a small quantity of cold fresh water. The relative displacement of the rods was monitored by two linear variable differential

120    transformer transducers (LVDTs, model: HBM WA2, with a measurement range and accuracy of 2 and $\pm 0.001$ mm, respectively). This relative displacement was used to determine the strain response of the specimen. As shown in Figures 2 and 3, the LVDTs were mounted on a rectangular steel placed across the basin.

The air temperature was kept at -10°C during all testing. To measure the through-thickness temperature gradient in all of the floating ice experiments, temperature probes were frozen into three 2.5 mm-diameter, 50 mm deep

125    holes were drilled on one side face of the specimen. As shown in a sketch of Figure 6a, one measurement point was in the middle of the specimen from the vertical direction, and the other two were 1.5 mm away from the upper and lower surfaces of the specimen, respectively. During each floating ice experiment, temperature readings from all three channels remained constant for the duration of the experiment, indicating that the thermal gradient was unaffected by the cyclic loading.

130    Figure 6b presents typical temperature profiles measured in two floating ice specimens. For the 5-ppt-saline floating ice, the temperature near the top surface, in the middle and near the bottom surface of the specimen was measured to be -3.0, -2.3 and -2.2°C, respectively, while the values were -3.1, -2.4 and -2.1°C, respectively, for the 7-ppt-saline ice floe. These temperature readings suggest that the average temperature of the floating ice was -2.5°C, much higher than the air temperature of the cold chamber (-10°C). The water temperature at five

135    centimeters below the water surface was measured to be $\approx$ -1.8°C in the floating ice tests.

The test matrix called for applying relatively low cyclic compressive stress levels with the system in load control. Figure 7 presents the loading waveforms used in the experiments and the test matrix is given in Table 1. In the experiments, the ice was first loaded with a linear ramp to reach an initial compressive stress level, at which point a compressive haversine waveform was immediately applied. In Figure 7a, $\sigma_{max}$ and $\sigma_{min}$ represent the upper and

140    the lower bounds of the cyclic compressive stress, respectively, and $T$ denotes the period for one loading cycle. As indicated by Table 1, six periods ranging from 1 to $10^3$ s were employed; these periods cover the main range of ocean wave periods, which usually vary from several seconds to tens of seconds (Reistad et al., 2011; Zijlema et al., 2012). In each dry test, only a fixed frequency was applied. Once the test was completed, the specimen recovered for 15 minutes before subsequent load cycles were applied. For all dry tests, the duration of the initial

145    loading ramp was fixed to be 1 s. In each of the tests corresponding to $T = 1, 5, 10$ and 100 s, 18 cycles were applied ($N = 18$), while for those with $T = 500$ and 1000 s, $N = 9$ and 4, respectively. The sequence of loading cycles was in ascending order of $T$ in all cases. As a time-saving measure, and to avoid freezing of the open water in the basin, cyclic stresses with increasing periods were applied continuously in the floating ice tests. The number of cycles for each period was as follows: $T = 1, 5$ or 10 s, $N = 10$, for $T = 100$ s, $N = 2$, and for $T = 500$ or 1000 s,

150    $N = 1$.

The cyclic compressive stress applied to the dry specimens varied from 0.08 to 0.25 MPa, which could be justifiably expected to not lead to severe damage of the specimen while being high enough to generate measurable strain (Cole and Dempsey, 2001). The stress in the floating experiments was lower, varying from 0.04 to 0.12 MPa, to avoid damage. For each case listed in Table 1, two specimens harvested from two ice sheets were subjected to each set of conditions. The specimens were named according to their salinity, test conditions (dry/floating), and the ice sheet from which it originated. For example, specimen name Dry-5ppt-1 indicates that it came from the first 5-ppt-saline ice sheet and was tested under the dry, isothermal conditions.

Figure 7b illustrates how the energy dissipation in the cyclic loading experiments was calculated. For common engineering materials subjected to uniaxial cyclic compression, the strain along the compressive direction versus the stress is usually characterized by hysteresis loops. The strain energy density dissipated in a loading cycle can be determined by integrating the stress-strain curve. As shown in Figure 7b, the area under the loading curve (region ABCF) represents the maximum strain energy input via the testing machine during a load cycle, and the area under region CDEF denotes the strain energy released during the unloading portion of the cycle. The energy density dissipation (EDD) in one full loading-unloading cycle is given by the difference between the areas of regions ABCF and CDEF (Liu et al., 2017, 2018). The energy density consumed in the hysteresis loop can, in general, be attributed to the internal friction and, in some cases, damage to the material. For each cycle, the energy dissipation rate (EDR) can be defined as the ratio of the dissipated energy to the input energy, namely the area of the region ABCDE divided by that of the region ABCF.

**3 Experimental results**

Figure 8 presents strain-time plots obtained from the dry experiments using specimen Dry-5ppt-1 under the indicated conditions. The strain-time curves manifest the following feature: If a line would be drawn through the maximum value for each cycle, the slope of the line would first decrease from its initial value for some number of cycles and then settle down to an almost constant value. This observation means that the strain response of the ice specimen under sinusoidal compressive stress reaches a relatively steady stage after the initial transient of the anelastic strain is exhausted, and that in this steady stage the accumulated viscous or permanent strain increases linearly with time. In addition, Figure 8 shows that the longer the period $T$ of cyclic loading, the larger the strain amplitude in one steady-stage cycle. The total amount of strain does not strictly increase with the loading period. This may be because the loading platen and the specimen did not always achieve perfect contact immediately,

causing some error in the strain measured in this initial stage of loading. Once intimate contact was achieved, the

180    measured strain became reliable.

Figure 9 shows the stress-strain curves for the same experiments. In each case, the area of the hysteresis loop for the first few cycles was comparatively large, and then gradually decreased to a constant value as the specimen reached the steady deformation stage described in the previous paragraph. For example, the hysteresis loops after the first stress cycle in the dry experiment with $T = 1000$ s are similar; $N = 4$ is enough for the dry specimen at $T$

185    $= 1000$ s to show steady-state response. Thus, the EDD (Figure 7b) decreases from its initial value to an approximately constant value. It is clear that the steady-state hysteresis loop area increase with the period of the cyclic loading, consistent with earlier studies (Cole, 1990; Murdza et al., 2018; Weber and Nixon, 1996).

Figures 10 and 11 display a set of strain-time plots and the corresponding stress-strain curves for the floating ice experiments on the 5-ppt-saline ice specimens, respectively. The curves in these two figures show similar features to those in Figures 8 and 9 for dry experiments: The floating ice also reached a steady state of deformation after

190    some loading cycles and the amplitude of the steady-state strain response still increased with $T$. Similar to the results of the dry experiments, Figure 11 indicates that the longer the loading period, the larger the strain increment of the floating specimen under one steady-state loading-unloading cycle. Comparison of Figures 9 and 11 in the steady state shows that, for constant $T$, both the strain increment per cycle and the area of one hysteresis loop, are

195    larger in the floating ice experiments than in the dry experiments even though the stress levels are lower than in the dry experiments. It is thus evident that the decreased stress levels in the floating ice experiments did not fully compensate for the temperature effects on the viscous and viscoelastic components of strain as, for example, the viscous strain rate of floating 5-ppt-saline ice specimen is fourteen times that of the corresponding dry specimen.

The energy density dissipation (EDD) and the energy dissipation rate (EDR) per cycle during steady-stage

200    deformation (Section 2.2 and Figure 7b) allow quantitative comparisons of the inelastic behavior of specimens as a function of test conditions. These are presented in Tables 2 and 3 for all, except the 1-second-period, experiments, for which the hysteresis loop areas are too small for accurate measurements. Tables 2 and 3 indicate that both the EDD and the EDR decrease with the increase of loading frequency. Moreover, under the same frequency, the 7-ppt-saline ice has larger EDD and EDR values than the 5-ppt-saline ice irrespective of the experiment type. In

205    addition, the floating ice experiments always exhibit higher EDD and EDR values than the dry experiments regardless of the ice salinities. The differences in the values of EDD are especially significant for low frequencies. For example, in the experiments with $T = 1000$ s, the average value of EDD for the 5-ppt-saline dry specimens is only 24% of that of the 5-ppt-saline floating specimens and 44% of that of the 7-ppt-saline dry specimens. However, for the experiments with $T = 5$ s, the average value of EDD in the former case is 47% and 77% of that in the latter

210    two cases, respectively. Thus, the ice salinity and the test conditions have a more significant influence on the energy dissipation of the ice when the cyclic loading period is long.

## 4 Material modeling

The hysteresis loops of the stress-strain curves manifest viscous and anelastic properties of the ice. According to previous studies (Cole, 1995; Leclair et al., 1999), in low-stress cyclic loading experiments, the microstructure of

215    the ice remains unaffected by loading, or in other words, no damage occurs within the material. In the present case of polycrystalline ice, the anelastic deformation is mainly attributed to two relaxation mechanisms, lattice dislocation relaxation and grain-boundary sliding. Viscous straining is attributable to basal dislocation glide. In this section, a dislocation-based model (Cole, 1995; Cole and Durell, 2001), which accounts for these mechanisms, is used to predict the strain response of the ice specimens based on their physical properties and experimental

220    conditions. Here the model is only briefly described, but a detailed description can be found from Cole et al. (1998), where the model is also demonstrated to reproduce the viscous and anelastic behavior of dry specimens. Here the applicability of the model in predicting the behavior of floating laboratory-prepared ice specimens subjected to cyclic loading is tested for the first time.

### 4.1 Brief description of the model

In the physically based model by Cole (1995) and Cole and Durell (2001), the axial strain, $\varepsilon$, of ice under uniaxial cyclic compression is considered to be composed of elastic, anelastic (delayed elastic) and viscous components, denoted here as $\varepsilon_e$, $\varepsilon_a$ and $\varepsilon_v$, respectively. The axial strain is expressed as

$$\varepsilon = \varepsilon_e + \varepsilon_a + \varepsilon_v. \tag{1}$$

230    In the case of sinusoidal stress waveform, $\varepsilon_e$ can be written as

$$\varepsilon_e = \frac{\sigma(\omega, t)}{E_0}, \tag{2}$$

where $\omega$ is the angular frequency of the stress waveform and $E_0$ is the unrelaxed modulus. Although detailed expressions have been developed for the effective elastic modulus as a function of crystallography, brine and gas porosity, and temperature, a simplified approach is adopted in the present effort. The anelastic component $\varepsilon_a$

235    incorporates both above-mentioned relaxation mechanisms to represent the time-dependent recoverable deformation. For the steady-stage deformation, $\varepsilon_a$ of ice subjected to sinusoidal compressive stress can be decomposed as (Cole and Dempsey 2001)

$$\varepsilon_a = \sigma(\omega, t) \left[ D_1^d(\omega) + D_2^d(\omega) + D_1^{gb}(\omega) + D_2^{gb}(\omega) \right], \tag{3}$$

where the compliance terms, $D$, with the superscripts "d" and "gb" denote the compliances induced by dislocation and grain boundary sliding, respectively. The compliance terms are defined as (Cole et al., 1998)

$$D_1^{\mathrm{d}}(\omega) = \delta D^{\mathrm{d}} \left\{ 1 - \frac{2}{\pi} \tan^{-1} \left[ e^{\left(\alpha^{\mathrm{d}} s^{\mathrm{d}}\right)} \right] \right\} \tag{4}$$

$$D_1^{\mathrm{gb}}(\omega) = \delta D^{\mathrm{gb}} \left\{ 1 - \frac{2}{\pi} \tan^{-1} \left[ e^{\left(\alpha^{\mathrm{gb}} s^{\mathrm{gb}}\right)} \right] \right\} \tag{5}$$

$$D_2^{\mathrm{d}}(\omega) = \alpha^{\mathrm{d}} \cdot \delta D^{\mathrm{d}} \frac{1}{e^{\left(\alpha^{\mathrm{d}} s^{\mathrm{d}}\right)} + e^{\left(-\alpha^{\mathrm{d}} s^{\mathrm{d}}\right)}} \tag{6}$$

$$D_2^{\mathrm{gb}}(\omega) = \alpha^{\mathrm{gb}} \cdot \delta D^{\mathrm{gb}} \frac{1}{e^{\left(\alpha^{\mathrm{gb}} s^{\mathrm{gb}}\right)} + e^{\left(-\alpha^{\mathrm{gb}} s^{\mathrm{gb}}\right)}} , \tag{7}$$

where $S^{\mathrm{d}} = \ln\left(\tau^{\mathrm{d}} \omega\right)$; $\tau^{\mathrm{d}}$ is the central relaxation time (Cole and Durell, 1995). $\alpha$ is a so-called peak broadening term, which accounts for the effect of a distribution in relaxation times of the basal plane dislocations. The grain boundary relaxation is calculated using similar mathematic expressions as the dislocation relaxation, but has a different strength, activation energy and peak-broadening term. The activation energy is 1.32 eV for the grain boundary relaxation and 0.55 eV for the dislocation relaxation (Cole and Dempsey, 2001). The peak-broadening terms for lattice dislocation relaxation and grain-boundary sliding relaxation are typically $\approx 0.5$ and 0.6, respectively, determined experimentally by Cole (1995), Cole and Dempsey (2001) and also validated by Heijkoop et al. (2018). The strength of the dislocation relaxation is calculated from

$$\delta D^{\mathrm{d}} = \frac{\rho \Omega b^2}{K} , \tag{8}$$

where $b$ represents Burgers vector ($b = 4.52 \times 10^{-10}$ m); $\rho$ denotes the mobile dislocation density, often found to be on the order of $10^9$ m$^{-2}$; $\Omega$ is an orientation factor, determining the average basal plane shear stress induced by the background normal stress ($\Omega = 1/\pi \approx 0.32$ for a horizontal specimen made of unaligned columnar ice (Cole, 1995)); $K$ is a restoring stress constant, determined as 0.07 kPa for polycrystalline ice in experiments (Cole and Durell 2001).

In Eq. (1), the viscous strain $\varepsilon_{\mathrm{v}}$ is often estimated with the following formulae (Cole and Durell, 2001):

$$\varepsilon_{\mathrm{v}} = \int_0^t \dot{\varepsilon}_{\mathrm{v}} d\bar{t} \tag{9}$$

$$\dot{\varepsilon}_{\mathrm{v}} = \frac{\beta \rho \Omega^{1.5} b^2 \sigma_{\mathrm{creep}}}{B_0} e^{\left(-\frac{Q_{\mathrm{glide}}}{kT^*}\right)} , \tag{10}$$

where $\beta = 0.3$, $Q_{glide} = 0.55$ eV, and $B_0 = 1.205 \times 10^{-9}$ Pa·s. $k$ is Boltzmann's constant, $T^*$ is the temperature in Kelvins. By using the above definitions and equations, the strain of the ice specimen can be finally determined via Eq. (1).

265

## 4.2 Modeling

In this study, the key quantity to be determined from the experiments is the dislocation density ($\rho$). With knowledge of the microstructure and orientation factor ($\Omega$), and given the experimental conditions, the anelastic term $\delta D^d$ and the viscous strain rate can be calculated directly. We opt here to determine $E_0$ empirically. These were done by

270    trial and error until the stress-strain curves generated by the model matched with those measured in the experiments with $T = 10$, 100 and 500 s. By making the slopes of the modeled and experimental hysteresis loops for $T = 10$ s comparable, $E_0$ could be determined. This is because the behavior of the specimens is mainly dominated by the un-relaxed modulus $E_0$ when the loading frequency is high (here 0.1 Hz to 1 Hz), as indicated in Figures 9 and 11. From Eqs. (9) and (10), one can find that the strain increment under one loading cycle is dependent on the

275    dislocation density $\rho$; based on this, the dislocation density $\rho$ was estimated by using the experimental results of $T = 100$ and 500 s and $\delta D^d$ was then determined from Eq. (8). $\delta D^{gb}$ was determined by referring to previous work (Cole 1995) because the grain boundary relaxation strength could be reasonably assumed constant for the ice material of interest here, and its effect on inelastic behavior of ice was significantly less than the dislocation mechanism. The values determined for the parameters are tabulated in Table 4. Subsequently, the model based on

280    these parameter values was applied to predict the test results for other loading periods. An example of the comparison of experimental and modeling results is presented in Figure 12, in which the steady-state strain curves from all dry experiments on the 5-ppt-saline ice specimen are accompanied by the simulated ones.

Figure 12 shows that the modeled strain records compare well with those from the experiments with period $T = 1$, 5 and 1000 s. The model reproduced the steady-state strain response of the specimens very well for all tested

285    frequencies. Figure 13 presents the stress-strain hysteresis loops from the same experiments together with those produced by the model. The hysteresis loops generated by using the model are very similar to those from the experiments. The loop area increases with $T$ in both the experiments and simulations.

For assessing the model in more detail, the values of EDD and EDR derived using it are given in Tables 5 and 6, respectively, and moreover, compared with the data from all the experiments (the test matrix is given in Table 1).

290    Tables 5 and 6 indicate that the model predicts well the values of EDD and EDR for all cyclic loading periods studied here. In general, the error in the predicted EDD and EDR values are within 20%, with the exception of only few cases. No obvious trend between the magnitude of error and loading period or experiment type was

observed. Note that for a given ice specimen, one dislocation density value adequately models the steady-state strain responses and energy dissipation values in tests conducted with different frequencies. The value of dislocation density, thus, remained constant through the cyclic loading.

**4.3 Further validation**

The above results show that the model can yield satisfactory predictions on the viscous and anelastic behavior of both dry and floating specimens. One may argue that the good agreement between the model predictions and the experimental results only indicates the capability of the model to predict the results for the experiments with the same stress levels as those used to calibrate the model parameters. To check whether the model can predict the results of the experiments with different stress levels than those above, additional experiments were performed on specimen Dry-5ppt-1 with higher stress (0.1–0.3 MPa) and on specimen Floating-7ppt-1 with lower stress (0.005–0.085 MPa) (Nominal cyclic stress of 0.005–0.085 MPa is low, but the setup could achieve it: With the accuracy of the system, the actual stress applied to the specimen was 0.005 ($\pm$0.001)–0.085 ($\pm$0.003) MPa). The model was then used to determine the strain response and energy dissipation in these tests using the parameterization based on the experiments of Section 3 (Table 4).

Figure 14 compares the stress-strain hysteresis loops obtained in the supplementary experiments with the predictions yielded from the model. Good agreement is observed between the predicted and measured hysteresis loops. Again, the relative errors in the EDD and EDR values are found to be less than 20% for most data sets. The model is, indeed, capable of predicting the deformation of saline ice in a dry environment or when floating in water irrespective of the stress level (given that the stress levels are moderate and do not cause an increase in dislocation density during deformation). The applicability of the model is highlighted by the fact that once the model parameters are calibrated through benchmark experiments (the elastic modulus and dislocation density in the present case), it yields sound predictions for the experiments conducted with other stress levels.

**5 Discussion**

Although past laboratory-scale work has provided insight into the mechanical behavior of sea ice, the work has been mostly performed using relatively cold, dry and isothermal specimens. The results above indicate that more attention should be paid to the mechanical behavior of relatively warm, floating ice with a naturally occurring temperature gradient. Here efforts were made to develop a relatively low-cost, convenient and useful approach for laboratory-scale floating ice experiments and for preparing small-scale, saline columnar ice specimens. The thin sections (Figures 4 and 5) indicated that the measures taken on the ice production guaranteed the generation of

non-oriented columnar ice. Moreover, the thin sections showed that the molds used for specimen preparation do not influence the columnar ice microstructure. This is encouraging, as molds are not often incorporated into growing sheets of non-oriented columnar ice. The use of molds in this way significantly simplified specimen preparation and resulted in accurate dimensions. The molds are especially effective in the experiments on floating ice specimens: The specimens thus produced have proper dimensions, require no cutting, have a realistic temperature gradient and can be quickly transferred to the test basin, so brine loss is minimized.

The results above are in qualitative agreement with what would be expected for floating ice, as for example, floating specimens having through thickness thermal gradient and mean temperature of -2.5°C exhibit lower modulus and more pronounced inelastic deformation in comparison with dry specimens at -10°C, as would be expected based on full-scale observations on the effect of temperature on this property (Timco and Weeks 2010; Cole 2020). This gives confidence on the methods employed in the production and mechanical testing of the specimens. Further, the good agreement between the results for floating ice and the corresponding model predictions show quantitative validity of the approach taken here. All-in-all, the results suggest that the chosen experimental techniques (including the loading system, the strain measurement scheme, the data acquisition system and settings) worked well and provided useful results for the analysis. An exception is some of the 1-second-period experiments, which yielded strain responses with unexpected features; this is because the hysteresis loop areas are very small in size, making accurate measurements with the used set-up challenging. This could be circumvented in the future experiments by using techniques and devices with even higher precision and setting a higher sampling rate of data acquisition. The methods proposed in this study to conduct laboratory experiments on floating ice experiments are practical and can provide a convenient approach for relatively low-cost experimentation on floating ice.

The laboratory work here not only demonstrated the availability of the proposed experimental methods, but also contributes to the understanding of the constitutive behavior of ice. A common trend in developing material models is to ensure they have a solid physical basis, that is, that they are based on an understanding of the physical processes that underlie the mechanical phenomena of interest. Above we used one such physically-based model introduced by Cole (1995). Earlier work, which has been based on the experiments resembling the dry experiments here, has shown that the model is capable of predicting the inelastic deformation of sea ice via dislocation-based mechanisms and is able to estimate the effective dislocation density in ice from experimental results. Here the model was successfully validated against the results from the floating ice experiments. Moreover, the results indicated that once the constant dislocation density value of the specimens was determined, the model adequately predicted the steady-stage deformation for the cyclic loading experiments conducted with different frequencies

and stress levels. Even if the use of floating specimens could be considered to only address the temperature profiles

355 of in-situ floating ice (with some other environmental conditions of natural ice floes ignored), the above results bring confidence to the model and demonstrate its potential in modeling practical applications involving ice in such conditions, especially considering that some research has been launched to devote to a numerical implementation of the model (O'Connor et al., 2020).

The good agreement between the experimental and modeling results also motivates discussion on the parameter

360 values in Table 4. Expectedly, the floating ice specimens have lower unrelaxed moduli than the dry specimen. For the 5-ppt and 7-ppt-saline ice, the average elastic modulus of the floating specimens is 66% and 55% lower than that of the dry specimens, respectively. In the dry experiments, the isothermal 7-ppt-saline ice has a 31% lower average elastic modulus than the 5-ppt-saline ice. In the floating ice experiments, the 7-ppt-saline specimen still has a lower average elastic modulus than the 5-ppt-saline specimen, but the difference, 8%, is not as prominent as

365 in the dry experiments. Thus, the fact that the ice was in contact with water and had a realistic temperature profile had a larger influence on the elastic modulus of ice than the variation of the ice salinities studied here.

Table 4 also indicates that the dislocation densities determined for the ice specimens were on the order of $\sim 10^8$– $10^{10}$ m$^{-2}$, and thus were in good agreement with values in the $10^9$ m$^{-2}$ order of magnitude given by Cole (1995). Moreover, the dislocation density of the floating ice was approximately one order of magnitude greater than that

370 of the dry specimen. Note that there is precedent showing the dislocation density of ice increasing with temperature (Cole and Durell, 2001; Cole, 2020). The same trend is seen here when the experiments change from dry specimens (-10°C) to relatively warm, floating, ones. In addition, the earlier work cited has shown that the dislocation density increases with the salinity. Therefore, the calculated dislocation densities make sense physically and are generally in line with expectations.

375 Specimens originating from two different ice sheets were tested. Table 4 shows that for a given set of conditions, the elastic modulus of the specimens showed only small variations from one sheet to another. Compared with the elastic modulus, the relative change in dislocation density was fairly large, which may be due to heterogeneity of ice. A similar degree of change in dislocation density was also reported by Cole and Durell (2001) related to dry, isothermal, ice specimens. As for the strength of the grain boundary relaxation, its value was taken as 2 (±1) ×10$^-$

380 $^{10}$ Pa$^{-1}$ for all specimens since variations in grain size among the ice specimens was small. Thus, here the main quantity to be determined from the experimental results for studying anelastic strain response of the specimens was the dislocation density. It was also found that for relatively high loading frequency (for example, 1 Hz used here), the modeled strain behavior was dominated by the un-relaxed modulus $E_0$, not sensitive to the dislocation

density or the strength of grain boundary relaxation. However, for low-frequency (0.001 Hz) cyclic loading, the modeled specimen deformation was very sensitive to the dislocation density.

The effect of water on the mechanical behavior of floating ice has also been attributed on temperature (Golden et al., 2007). Moreover, the specimens harvested from floating ice sheets lose brine once removed from the sheet; warm ice in particular can lose a significant amount of brine which could significantly alter the mechanical properties in subsequent experiments. In addition, some remaining brine (for example, some of those in capillary brine channels) must freeze during the storage process of dry specimens; this may as well lead to some difference in the macroscopic mechanical behavior (for example, in elastic modulus) of dry and floating specimens (Marchenko and Lishman, 2017; Eicken, 1992; Jones et al., 2012; Gough et al., 2012). The methodology developed in the present effort avoids such problems and is expected to produce more realistic mechanical behavior, particularly when interest centers on behavior at relatively warm temperatures where brine drainage is extensive.

The analysis and modeling indicated that the physical mechanisms of deformation in both the warmer, floating specimens and the colder dry specimens were essentially the same. Warmer saline ice had a smaller modulus due to its higher liquid brine volume, which necessarily decreases the volume of the solid ice matrix (thereby reducing the bulk elastic modulus) and there is a pronounced increase in the effective $\rho$ with increasing temperature (Cole and Durell, 2001; Timco and Weeks, 2010; Cole, 2020).

## 6 Conclusions

Equipment and methods were developed to conduct laboratory experiments to examine the mechanical properties of floating saline ice specimens with a naturally occurring temperature gradient. In this initial effort, we examined the strain response of floating saline ice under cyclic compressive stresses and conducted reference experiments under dry, isothermal conditions. The experiments examined specimens having one of two nominal salinities (5 and 7 ppt), cyclic loading frequencies from $10^{-3}$ to 1 Hz were applied and two levels of cyclic stress were applied. The experimental results compared favorably with the theoretical predictions obtained using a physically based constitutive model for saline ice. Given the limitations of the experiments program, the following conclusions can be drawn.

Equipment and methods:

1. Groups of unaligned, columnar grained saline ice specimens can be produced simultaneously in the laboratory using floating molds, and the presence of the molds has no observable effect on their microstructure.

2. The use of molds produced specimens that could be placed directly in the mechanical testing fixture, which for the case of floating ice experiments, provided a way to maintain a realistic temperature gradient during subsequent experimentation.

3. The experimental apparatus, which employed an electrohydraulic actuator and a saline water tank placed in a cold room, provided a way to apply in-plane loads to floating ice specimens and successfully produced monotonic and cyclic loading waveforms employed in more conventional systems.

Constitutive modeling:

4. The dislocation mechanics of the model employed in the analysis can reproduce well the strain response and energy dissipation of saline ice subjected to cyclic loading for floating ice or dry specimens, and for the observed ice salinities. The results show that the prediction errors of the energy density dissipation and the energy release rate are within $\approx 20\%$.

5. For either dry or floating specimens, the higher the salinity of ice, the lower the modulus ($E_0$) and the larger the dislocation density ($\rho$). In addition, $E_0$ is much higher and $\rho$ is far smaller for the dry specimens than for the floating specimens, provided other experimental variables are consistent.

This work makes it clear that the mechanical behavior of floating specimens of saline ice can be examined in the laboratory under a reasonable approximation of in-situ conditions and with good efficiency. This capability opens the door to more sophisticated experimental work on saline ice under more realistic environmental conditions than previously possible.

**Financial support:** The authors are grateful for the financial support from the Academy of Finland through the project (309830) Ice Block Breakage: Experiments and Simulations (ICEBES).

**Acknowledgments:** The authors thank the help from the technical staff of Aalto University Department of Mechanical Engineering, and especially, from Kari Kantola and Veijo Laukkanen.

435 **Author contributions:** AP, MW and DMC designed the study. MW and MP performed the experiments. MW, AP and DMC contributed to the interpretation of the results. MW, AP and DMC drafted the paper. All authors commented on the text.

**Code and data availability:** The code used for material modeling is written in MATLAB. Scripts used for analysis and more detailed information of the experimental results are available from the authors upon request.

440 **Competing interests:** The authors declare that they have no conflict of interest.

**References**

Blockley, E. W. and Peterson, K. A.: Improving Met Office seasonal predictions of Arctic sea ice using assimilation of CryoSat-2 thickness, The Cryosphere, 12, 3419–3438, https://doi.org/10.5194/tc-12-3419-2018, 2018.

Boe, J. L., Hall, A., and Qu X.: September sea-ice cover in the Arctic Ocean projected to vanish by 2100, Nat.
445 Geosci., 2, 341–343, doi:10.1038/ngeo467, 2009.

Bond, P. E. and Langhorne, P. J.: Fatigue behavior of cantilever beams of saline ice, J. Cold Reg. Eng., 11, 99–112, https://doi.org/10.1061/(ASCE)0887-381X(1997)11:2(99), 1997.

Cheng, S., Tsarau, A., Evers, K. U., and Shen, H.: Floe size effect on gravity wave propagation through ice covers, J. Geophys. Res.-Oceans, 124, 320–334, https://doi.org/ 10.1029/2018JC014094, 2019.

450 Cole, D. M.: Reversed direct-stress testing of ice: Initial experimental results and analysis. Cold Reg. Sci. Technol., 18, 303–321, https://doi.org/10.1016/0165-232X(90)90027-T,1990.

Cole, D. M.: A model for the anelastic straining of saline ice subjected to cyclic loading, Philos. Mag. A, 72, 231–248, https://doi.org/10.1080/01418619508239592, 1995.

Cole, D. M.: On the physical basis for the creep of ice: the high temperature regime. J. Glaciol., 1–14.
455 https://doi.org/10.1017/jog.2020.15, 2020.

Cole, D. M. and Dempsey, J. P.: Influence of scale on the constitutive behavior of sea ice, In: International Union of Theoretical and Applied Mechanics Symposium on Scaling Laws in Ice Mechanics and Ice Dynamics, pp. 251–264. Kluwer, Dordrecht, https://doi.org/10.1007/978-94-015-9735-7_22, 2001.

Cole, D. M. and Dempsey, J. P.: In situ sea ice experiments in McMurdo Sound: cyclic loading, fracture, and
460 acoustic emissions, J. Cold Reg. Eng., 18, 155–174, https://doi.org/10.1061/(ASCE)0887-381X(2004)18:4(155), 2004.

Cole, D. M. and Durell, G. D.: The cyclic loading of saline ice, Philos. Mag. A, 72, 209–229, https://doi.org/10.1080/01418619508239591, 1995.

Cole, D. M. and Durell, G. D.: A dislocation-based analysis of strain history effects in ice, Philos. Mag. A, 81, 1849–1872, https://doi.org/10.1080/01418610108216640, 2001.

Cole, D. M., Johnson, R. A., and Durell, G. D.: Cyclic loading and creep response of aligned first-year sea ice, J. Geophys. Res., 103, 21,751–21,758S, https://doi.org/10.1029/98JC01265, 1998.

Dempsey, J. P.: Research trends in ice mechanics, Int. J. Solids Struct., 37, 131–153, https://doi.org/10.1016/S0020-7683(99)00084-0, 2000.

Dempsey, J. P., Adamson, R. M., and Mulmule. S. V.: Scale effects on the in-situ tensile strength and fracture of ice, Part II: First-year sea ice at Resolute, N.W.T. Int. J. Fract., 95, 347–366, https://doi.org/10.1023/A:1018650303385, 1999.

Dempsey, J. P., Cole, D. M., and Wang, S.: Tensile fracture of a single crack in first-year sea ice. Phil. Trans. R. Soc. A, 376, https://doi.org/10.1098/rsta.2017.0346, 2018,

Eicken, H.: Salinity profiles of Antarctic sea ice: Field data and model results, J. Geophys. Res.-Oceans, 97, 15,545–15,557, https://doi.org/10.1029/92JC01588, 1992.

Feltham, D. L.: sea Ice rheology. Annu. Rev. Fluid Mech., 40, 91–112, https://doi.org/10.1146/annurev.fluid.40.111406.102151, 2008.

Gagne, M. E., Gillett N. P., and Fyfe, J. C.: Observed and simulated changes in Antarctic sea ice extent over the past 50 years, Geophys. Res. Lett., 42, 90–95, https://doi.org/10.1002/2014GL062231, 2015.

Golden, K. M., Eicken, H., Heaton, A. L., Miner, J., Pringle, D. J., and Zhu, J.: Thermal evolution of permeability and microstructure in sea ice, Geophys. Res. Lett., 34, L16501, https://doi.org/10.1029/2007GL030447, 2007.

Gough, A. J., Mahoney, A. R., Langhorne, P. J., Williams, M. J. M., and Haskell, T. G.: Sea ice salinity and structure: A winter time series of salinity and its distribution, J. Geophys. Res.-Oceans, 7, C03008, https://doi.org/10.1029/2011JC007527, 2012.

Gow, A. J. Crystalline structure of urea ice sheets used in modeling experiments in the CRREL test basin. CRREL report ; 84-24, https://hdl.handle.net/11681/9553, 1984.

Haskell, T. G., Robinson, W. H., and Langhorne, P. J.: Preliminary results from fatigue tests on in situ sea ice beams, Cold Reg. Sci. Technol., 24, 167–176, https://doi.org/10.1016/0165-232X(95)00015-4, 1996.

Heijkoop, A. N., Nord, T. S., and Høyland, K. V.: Strain-controlled cyclic compression of sea ice. 24th IAHR International Symposium on Ice Vladivostok, Russia, June 4 to 9, 2018.

Herman, A., Cheng, S., and Shen, H. H.: Wave energy attenuation in fields of colliding ice floes – Part 1: Discrete-element modelling of dissipation due to ice–water drag, The Cryosphere, 13, 2887–2900, https://doi.org/10.5194/tc-13-2887-2019, 2019a.

Herman, A., Cheng S., and Shen, H. H.: Wave energy attenuation in fields of colliding ice floes – Part 2: A laboratory case study, The Cryosphere, 13, 2901–2914, https://doi.org/10.5194/tc-13-2901-2019, 2019b.

Iliescu, D. and Schulson, E. M.: Brittle compressive failure of ice: monotonic versus cyclic loading, Acta Mater., 50, 2163–2172, https://doi.org/10.1016/S1359-6454(02)00060-5, 2002.

Iliescu, D., Murdza, A., Schulson, E. M., and Renshaw, C. E.: Strengthening ice through cyclic loading, J. Glaciol., 63, 663–669, https://doi.org/10.1017/jog.2017.32, 2017.

Jones, K. A., Ingham, M., and Eicken, H. Modeling the anisotropic brine microstructure in first‐year arctic sea ice, J. Geophys. Res.-Oceans, 117, C02005, doi:10.1029/2011JC007607, 2012.

Kartashkin, B. D.: Experimental studies of the physico-mechanical properties of ice, Tsentra'nyy
505        Aerogidrodinamicheskiy Institut, 1947

Kern, S., Lavergne, T., Notz, D., Pedersen, L. T., Tonboe, R. T., Saldo, R., and Sørensen, A. M. D.: Satellite passive
microwave sea-ice concentration data set intercomparison: closed ice and ship-based observations, The
Cryosphere, 13, 3261–3307, https://doi.org/10.5194/tc-13-3261-2019, 2019.

Langway, C. C.: Ice fabrics and the universal stage, Report # 62, CRREL, 1958.

510    Langhorne, P. J., Squire, V. A., Fox, C., and Haskell, T. G.: Break-up of sea ice by ocean waves, Ann. Glaciol., 27,
438–442, https://doi.org/10.3189/S0260305500017869, 1998.

Langhorne, P. J., Hughes, K. G., Gough, A. J., Smith, I. J., Williams, M. J. M., Robinson, N. J., Stevens, C. L.,
Rack, W., Price, D., Leonard, G. H., Mahoney, A. R., Haas, C., and Haskell, T. G.: Observed platelet ice
distributions in Antarctic sea ice: An index for ocean-ice shelf heat flux, Geophys. Res. Lett., 42, 5442–
515        5451, https://doi.org/10.1002/2015GL064508, 2015.

Leclair, E. S., Schapery, R. A., and Dempsey, J. P.: A broad-spectrum constitutive modeling technique applied to
saline ice, Int. J. Fract., 97, 209–226, https://doi.org/10.1023/A:1018358923672, 1999.

Li, J., Kohout, A. L., and Shen, H. H.: Comparison of wave propagation through ice covers in calm and storm
conditions, Geophys. Res. Lett., 42, 5935–5941, https://doi.org/10.1002/2015GL064715, 2015.

520    Li, Z., Riska, K.: Preliminary study of physical and mechanical properties of model ice. Technical Report M-212.
Helsinki University of Technology, 1996.

Liu, Y., Dai, F., Dong, L., Xu N., and Feng, P.: Experimental investigation on the fatigue mechanical properties of
intermittently jointed rock models under cyclic uniaxial compression with different loading parameters,
Rock Mech. Rock Eng., 51, 47–68, https://doi.org/10.1007/s00603-017-1327-7, 2018.

525    Liu, Y., Dai, F., Fan, P., Xu, N., and Dong, L.: Experimental investigation of the influence of joint geometric
configurations on the mechanical properties of intermittent jointed rock models under cyclic uniaxial
compression, Rock Mech. Rock Eng., 50, 453–1471, https://doi.org/10.1007/s00603-017-1190-6, 2017

Lu, W. and Løset, S.: Parallel channels' fracturing mechanism during ice management operations. Part II:
Experiment, Cold Reg. Sci. Technol., 156, 117–133, https://doi.org/10.1016/j.coldregions.2018.07.011,
530        2018.

Lu, W., Lubbad, R., Shestov, A., and Løset, S.: Parallel channels' fracturing mechanism during ice management
operations, Part I: Theory. Cold Reg. Sci. Technol., 156, 102–116,
https://doi.org/10.1016/j.coldregions.2018.07.010, 2018.

Marchenko, A. and Lishman, B.: The influence of closed brine pockets and permeable brine channels on the
535        thermo-elastic properties of saline ice. Phil. Trans. R. Soc. A, 375, 20150351,
http://dx.doi.org/10.1098/rsta.2015.0351, 2017.

Mellor, M. and Cole, D.: Cyclic loading and fatigue in ice. Cold Reg. Sci. Technol., 4, 41-53,
https://doi.org/10.1016/0165-232X(81)90029-X, 1981.

Murdza, A., Schulson, E. M., and Renshaw, C. E.: Hysteretic behavior of freshwater ice under cyclic loading: A
540        preliminary results. 24th IAHR International Symposium on Ice. Vladivostok, 185–192, 2018.

Murdza, A., Schulson, E. M., and Renshaw, C. E.: The effect of cyclic loading on the flexural strength of columnar
freshwater ice. In the Proceedings of the 25th International Conference on Port and Ocean Engineering
under Arctic Conditions (POAC'19). Electronic publication, 2019.

O'Connor DT, West BA, Haehnel RB, Asenath-Smith E, Cole D. A viscoelastic integral formulation and numerical implementation of an isotropic constitutive model of saline ice, Cold Reg. Sci. Technol., 171, 102983, https://doi.org/10.1016/j.coldregions.2019.102983, 2020.

Polojärvi, A., Tuhkuri, J., and Pustogvar, A. DEM simulations of direct shear box experiments of ice rubble: Force chains and peak loads, Cold Reg. Sci. Technol., 116, 12–23, https://doi.org/10.1016/j.coldregions.2015.03.011, 2015.

Ranta, J., Polojärvi, A., and Tuhkuri, J. The statistical analysis of peak ice loads in a simulated ice-structure interaction process, Cold Reg. Sci. Technol., 133, 46–55, https://doi.org/10.1016/j.coldregions.2016.10.002, 2017.

Ranta, J., Polojärvi, A., and Tuhkuri, J.: Ice loads on inclined marine structures - Virtual experiments on ice failure process evolution, Mar. Struct., 57, 72–86, https://doi.org/10.1016/j.marstruc.2017.09.004, 2018a.

Ranta, J., Polojärvi, A., and Tuhkuri, J.: Limit mechanisms for ice loads on inclined structures: Buckling, Cold Reg. Sci. Technol., 147, 34–44, https://doi.org/10.1016/j.coldregions.2017.12.009, 2018b.

Reistad, M., Breivik, Ø., Haakenstad, H., Aarnes, O. J., Furevik, B. R., and Bidlot, J. R.: A high-resolution hindcast of wind and waves for the North Sea, the Norwegian Sea, and the Barents Sea, J. Geophys. Res., 116, C05019, https://doi.org/10.1029/2010JC006402, 2011.

Ridley, J. K. and Blockley, E. W.: Brief communication: Solar radiation management not as effective as $CO_2$ mitigation for Arctic sea ice loss in hitting the 1.5 and 2 °C COP climate targets, The Cryosphere, 12, 3355–3360, https://doi.org/10.5194/tc-12-3355-2018, 2018.

Schulson, E. M. and Duval, P.: Creep and fracture of ice, Cambridge University Press, Cambridge, 2009.

Serreze, M. C. and Stroeve, J.: Arctic sea ice trends, variability and implications for seasonal ice forecasting, Phil. Trans. R. Soc. A, 373, 20140159, http://dx.doi.org/10.1098/rsta.2014.0159, 2015.

Smith, I. J., Gough, A. J., Langhorne, P. J., Mahoney, A. R., Leonard, G. H., Van Hale, R., Jendersie, S., and Haskellf, T. G.: First-year land-fast Antarctic sea ice as an archive of ice shelf meltwater fluxes, Cold Reg. Sci. Technol., 113, 63–70, https://doi.org/10.1016/j.coldregions.2015.01.007, 2015.

Tabata, T. and Nohguchi, Y.: Failure of sea ice by repeated compression, In: Tryde P. (eds) Physics and Mechanics of Ice, International Union of Theoretical and Applied Mechanics, Springer, Berlin, Heidelberg, 351–362, https://doi.org/10.1007/978-3-642-81434-1_25, 1980.

Timco, G. W. and Weeks, W. F.: A review of the engineering properties of sea ice, Cold Reg. Sci. Technol., 60, 107–129, https://doi.org/10.1016/j.coldregions.2009.10.003, 2010.

Tuhkuri, J. and Polojärvi, A.: A review of discrete element simulation of ice-structure interaction, Phil. Trans. R. Soc. A, 376, 20170335, http://dx.doi.org/10.1098/rsta.2017.0335, 2018.

Vincent, M. R. and Dempsey, J. P.: Servo-hydraulic pin loading device (HPLD) for in situ ice testing, J. Cold Reg. Eng., 13, 21–36, https://doi.org/10.1061/(ASCE)0887-381X(1999)13:1(21), 1999.

Voermans, J. J., Babanin, A. V., Thomson, J., Smith, M. M., and Shen, H. H.: Wave attenuation by sea ice turbulence, Geophys. Res. Lett., 46, 6796–6803, https://doi.org/10.1029/2019GL082945, 2019.

Weber, L. J. and Nixon, W. A.: Hysteretic behavior in ice under fatigue loading. Proceedings of the 15th International Conference on Offshore Mechanics and Arctic Engineering. 75–82, 1996.

Wongpan, P., Hughes, K. G., Langhorne, P. J., and Smith, I. J.: Brine Convection, temperature fluctuations, and permeability in winter Antarctic land-fast sea ice, 123, 216–230, https://doi.org/10.1002/2017JC012999, 2018.

585  Zijlema, M., Vledder, G. Ph. van, and Holthuijsen, L. H.: Bottom friction and wind drag for wave models, Coast. Eng., 65, 19–26, https://doi.org/10.1016/j.coastaleng.2012.03.002, 2012.

**Table 1 The test matrix of this experimental campaign. The campaign included two test types, two ice salinities, five periods and two test-type-dependent load levels. For each case, two specimens harvested from two ice sheets were tested.**

| Case | Specimen no. | Ice salinity (ppt) | Dry/Floating | Average ice temperature (℃) | Period (s) | Cyclic compressive Stresses (MPa) |
|---|---|---|---|---|---|---|
| I | Dry-5ppt-1, Dry-5ppt-2 | 5 | Dry | -10 | 1, 5, 10, 100, 500, 1000 | 0.08–0.25 |
| II | Dry-7ppt-1, Dry-7ppt-2 | 7 | Dry | -10 | 1, 5, 10, 100, 500, 1000 | 0.08–0.25 |
| III | Floating-5ppt-1, Floating-5ppt-2 | 5 | Floating | -2.5 | 1, 5, 10, 100, 500, 1000 | 0.04–0.12 |
| IV | Floating-7ppt-1, Floating-7ppt-2 | 7 | Floating | -2.5 | 1, 5, 10, 100, 500, 1000 | 0.04–0.12 |

**Table 2 The energy density (J·m$^{-3}$) dissipated in a typical loading-unloading cycle of each experiment.**

| Specimen no. | Frequency (Hz) | | | | |
|---|---|---|---|---|---|
| | 0.001 | 0.002 | 0.01 | 0.1 | 0.2 |
| Dry-5ppt-1 | 8.83 | 5.44 | 2.01 | 0.67 | 0.71 |
| Dry-5ppt-2 | 5.36 | 2.93 | 1.57 | 0.54 | 0.36 |
| Dry-7ppt-1 | 14.4 | 7.16 | 2.87 | 0.91 | 0.66 |
| Dry-7ppt-2 | 20.8 | 14.0 | 7.80 | 2.49 | 2.05 |
| Floating-5ppt-1 | 25.0 | 15.4 | 4.78 | 0.85 | 0.63 |
| Floating-5ppt-2 | 28.4 | 16.2 | 4.79 | 0.91 | 0.54 |
| Floating-7ppt-1 | 151 | 67.7 | 20.2 | 3.85 | 2.52 |
| Floating-7ppt-2 | 63.6 | 38.3 | 11.7 | 2.40 | 1.63 |

**Table 3 The energy dissipation rate (%) in a typical loading-unloading cycle of each experiment.**

| Specimen no. | Frequency (Hz) | | | | |
|---|---|---|---|---|---|
| | 0.001 | 0.002 | 0.01 | 0.1 | 0.2 |
| Dry-5ppt-1 | 48.3 | 40.2 | 22.0 | 9.86 | 9.93 |
| Dry-5ppt-2 | 35.4 | 22.7 | 17.6 | 8.68 | 5.50 |
| Dry-7ppt-1 | 55.6 | 37.3 | 21.6 | 11.0 | 8.60 |
| Dry-7ppt-2 | 55.7 | 44.7 | 32.3 | 16.0 | 14.3 |
| Floating-5ppt-1 | 89.6 | 76.1 | 44.2 | 15.5 | 11.8 |
| Floating-5ppt-2 | 87.7 | 69.8 | 39.4 | 17.4 | 11.3 |
| Floating-7ppt-1 | 98.3 | 91.7 | 70.5 | 32.0 | 25.1 |
| Floating-7ppt-2 | 88.1 | 76.0 | 56.4 | 26.3 | 20.2 |

590

595

**Table 4. Values of the model parameters calibrated for simulating the strain response of the ice specimens (in Section 5, these values are discussed and compared to those reported in references).**

| Specimen no. | Elastic modulus $E_0$ (GPa) | Dislocation density $\rho$ (m$^{-2}$) | Strength of dislocation relaxation $\delta D^d$ (Pa$^{-1}$) | Strength of grain boundary $\delta D^{gb}$ (Pa$^{-1}$) |
|---|---|---|---|---|
| Dry-5ppt-1 | 6.0 | $7.53\times10^8$ | $7\times10^{-10}$ | $1\times10^{-10}$ |
| Dry-5ppt-2 | 5.6 | $4.31\times10^8$ | $4\times10^{-10}$ | $1\times10^{-10}$ |
| Dry-7ppt-1 | 4.0 | $1.18\times10^9$ | $1.1\times10^{-9}$ | $1\times10^{-10}$ |
| Dry-7ppt-2 | 4.0 | $1.83\times10^9$ | $1.7\times10^{-9}$ | $3\times10^{-10}$ |
| Floating-5ppt-1 | 2.0 | $5.92\times10^9$ | $5.5\times10^{-9}$ | $3\times10^{-10}$ |
| Floating-5ppt-2 | 1.9 | $6.46\times10^9$ | $6\times10^{-9}$ | $1\times10^{-10}$ |
| Floating-7ppt-1 | 1.9 | $2.58\times10^{10}$ | $2.4\times10^{-8}$ | $3\times10^{-10}$ |
| Floating-7ppt-2 | 1.7 | $1.40\times10^{10}$ | $1.3\times10^{-8}$ | $2\times10^{-10}$ |

600

**Table 5. Modeling results of the strain energy density (J·m$^{-3}$) dissipated per loading-unloading cycle (the values given in parentheses are error percentages of model predictions relative to experimental results).**

| Specimen no. | Frequency | | | | |
|---|---|---|---|---|---|
| | 0.001 Hz | 0.002 Hz | 0.01 Hz | 0.1 Hz | 0.2 Hz |
| Dry-5ppt-1 | 9.12 (7%) | 5.16 (9%) | 1.74 (-10%) | 0.69 (-9%) | 0.68 (-21%) |
| Dry-5ppt-2 | 5.22 (-3%) | 3.10 (6%) | 1.15 (-27%) | 0.55 (2%) | 0.33 (-8%) |
| Dry-7ppt-1 | 15.1 (5%) | 8.76 (22%) | 2.65 (-8%) | 0.86 (-5%) | 0.79 (20%) |
| Dry-7ppt-2 | 21.9 (-1%) | 12.5 (-4%) | 6.44 (-9%) | 2.00 (-22%) | 1.97 (12%) |
| Floating-5ppt-1 | 27.0 (8%) | 14.9 (-3%) | 4.05 (-15%) | 0.91 (7%) | 0.73 (16%) |
| Floating-5ppt-2 | 30.3 (3%) | 16.8 (1%) | 4.58 (-6%) | 0.89 (-17%) | 0.61 (-8%) |
| Floating-7ppt-1 | 125 (-17%) | 68.5 (1%) | 18.6 (-8%) | 3.79 (-2%) | 2.58 (2%) |
| Floating-7ppt-2 | 65.4 (-17%) | 36.4 (-4%) | 10.0 (-21%) | 2.18 (10%) | 1.73 (13%) |

605

**Table 6. Modeling results of the strain energy dissipation rate (%) per loading-unloading cycle (the values given in parentheses are error percentages of model predictions relative to experimental results).**

| Specimen no. | Frequency | | | | |
|---|---|---|---|---|---|
| | 0.001 Hz | 0.002 Hz | 0.01 Hz | 0.1 Hz | 0.2 Hz |
| Dry-5ppt-1 | 49.2 (4%) | 36.7 (-1%) | 18.5 (-13%) | 9.43 (-12%) | 9.81 (-16%) |
| Dry-5ppt-2 | 37.4 (16%) | 25.9 (14%) | 13.9 (-21%) | 7.5 (-5%) | 5.70 (12%) |
| Dry-7ppt-1 | 53.1 (-1%) | 41.3 (-2%) | 20.2 (10%) | 8.99 (-18%) | 8.50 (12%) |
| Dry-7ppt-2 | 51.3 (-1%) | 38.9 (-2%) | 25.7 (10%) | 12.6 (-18%) | 13.9 (12%) |
| Floating-5ppt-1 | 87.8 (-5%) | 77.1 (-4%) | 40.0 (-15%) | 16.0 (3%) | 14.0 (3%) |
| Floating-5ppt-2 | 91.1 (-1%) | 82.0 (6%) | 45.1 (-4%) | 17.6 (9%) | 13.4 (26%) |
| Floating-7ppt-1 | 86.4 (-1%) | 77.4 (-3%) | 59.9 (-10%) | 34.0 (13%) | 28.2 (17%) |
| Floating-7ppt-2 | 94.5 (-1%) | 88.3 (-3%) | 52.9 (-10%) | 23.8 (13%) | 20.5 (17%) |
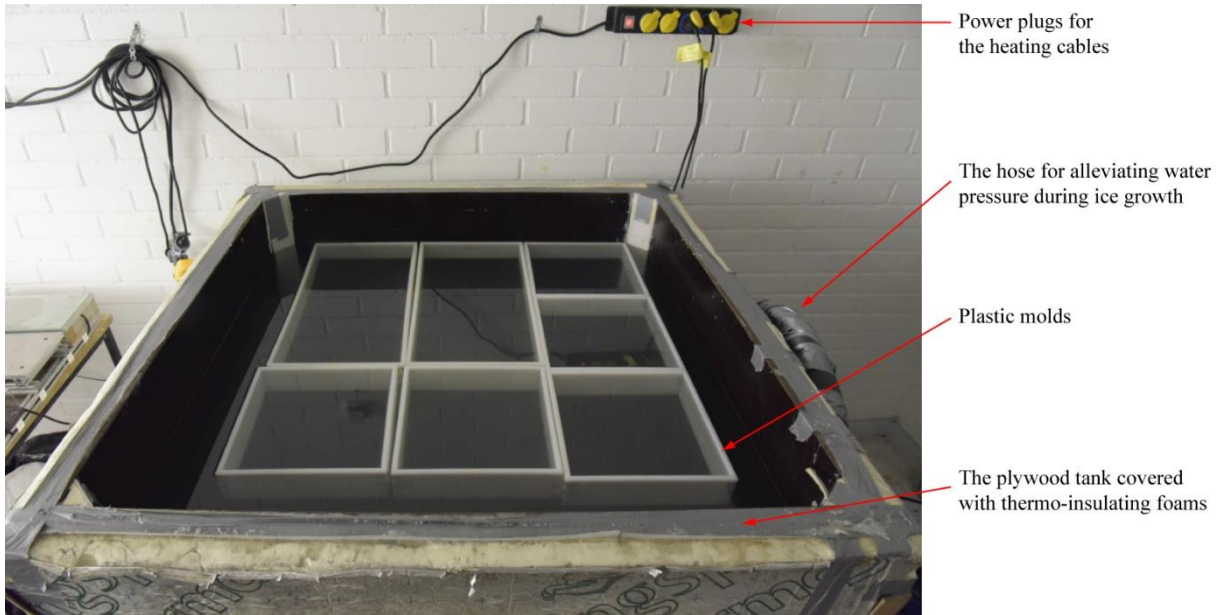
**Figure 1. The tank made of plywood for growing ice specimens.**

(a)                                        (b)

**Figure 2. Equipment used in the (a) dry and (b) floating ice experiments. One of the plastic molds used when growing ice is shown in (b). The thin ice cover of the basin, seen in (b), was broken before performing the**
 **experiments.**

Power plugs for
the heating cables

The hose for alleviating water
pressure during ice growth

Plastic molds

The plywood tank covered
with thermo-insulating foams
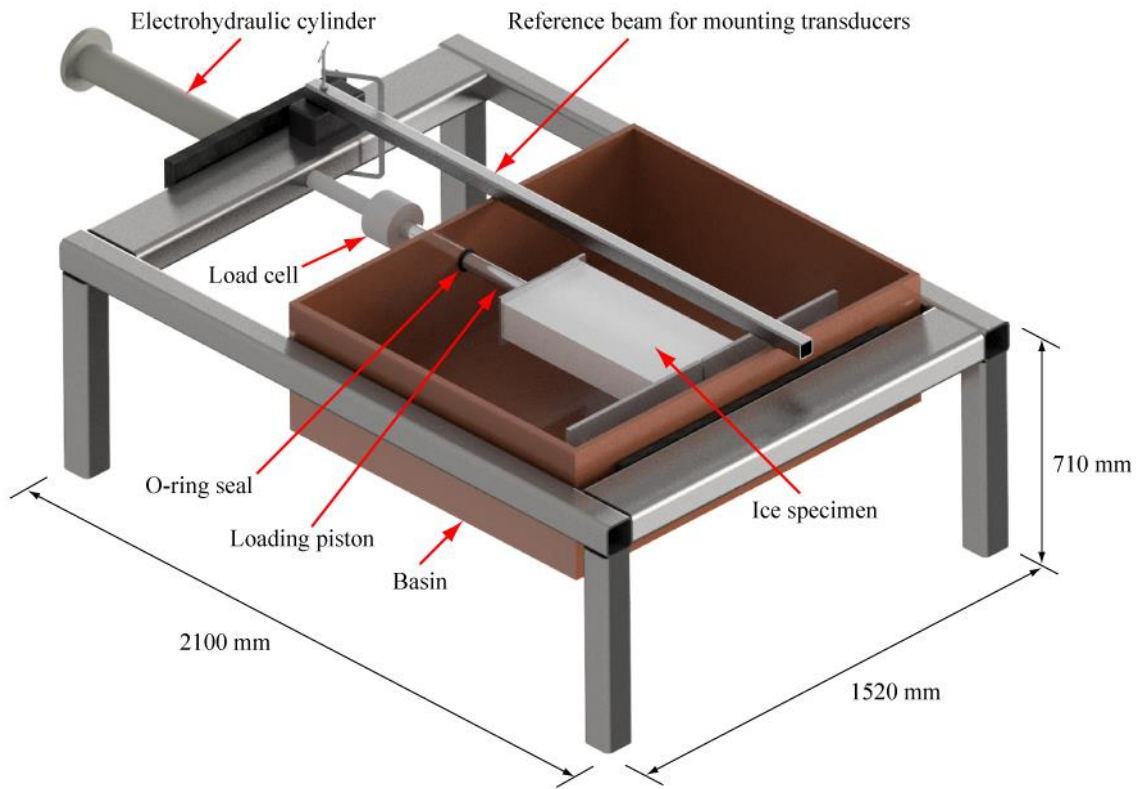
**Figure 3. A sketch of the test rig used in the experiments. The inner dimensions of the basin are 1320 mm × 1280 mm × 400 mm.**

620
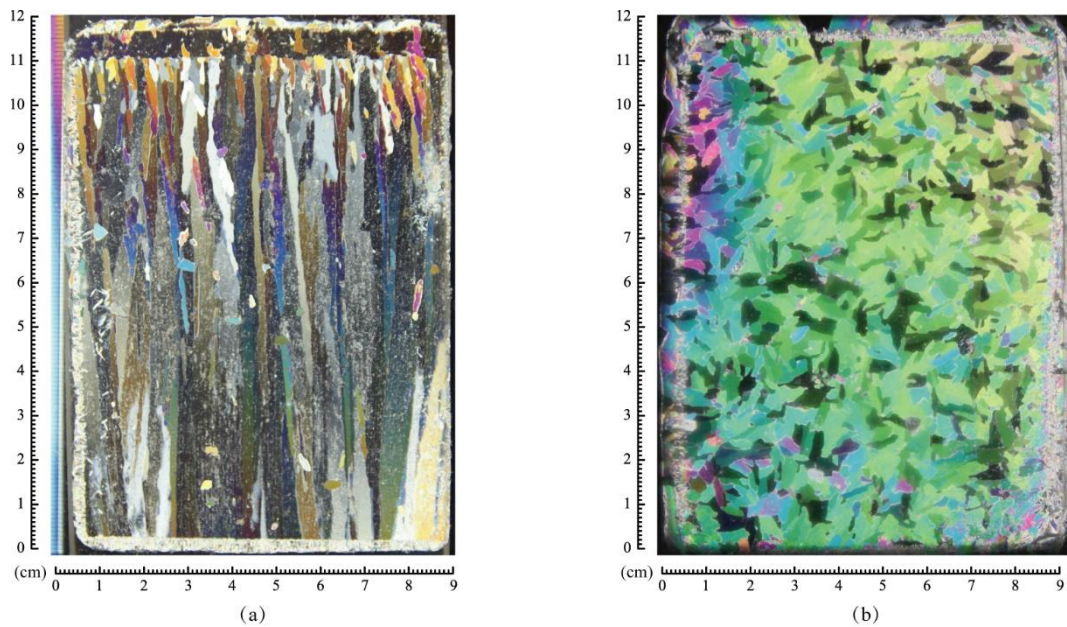
**Figure 4. One set of thin sections of the ice (salinity: 5 ppt) grown in this experimental campaign: (a) vertical; (b) horizontal.**

625
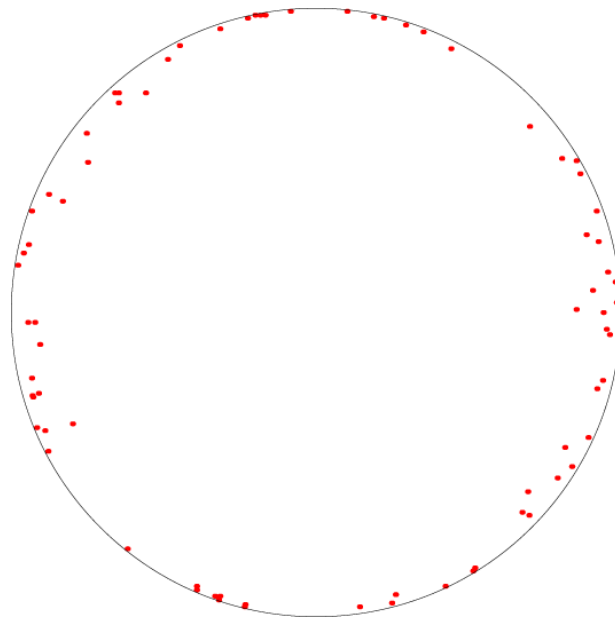
**Figure 5. A typical Schmidt equal area net pole projection drawn on the basis of grain orientations.**

(a)                                                            (b)
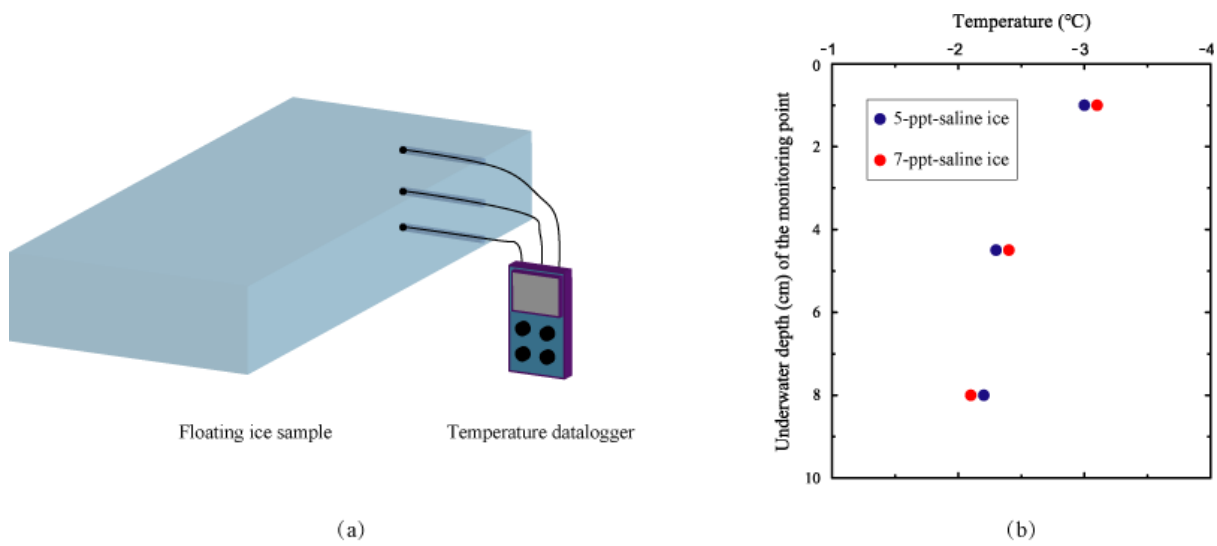
630 **Figure 6. Monitoring of the through-thickness thermal gradient of floating ice: (a) a schematic diagram of the arrangement of the temperature probes and (b) the measured through-thickness thermal gradient inside two floating ice specimens.**

(a)                                          (b)
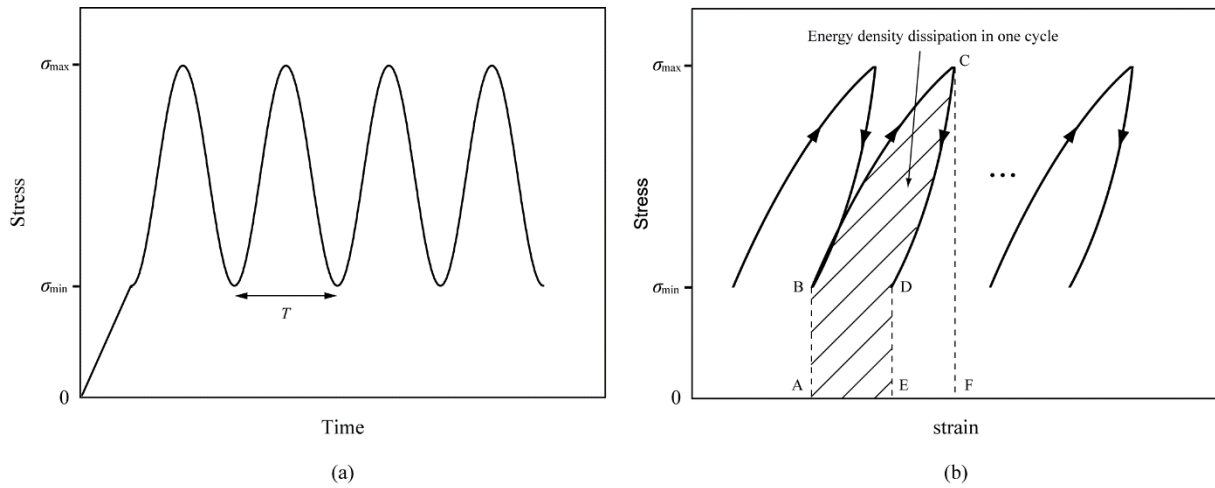
**Figure 7. Schematic diagrams of the cyclic loads: (a) the inputted stress waveform, and (b) the method for calculating the energy density dissipated in one loading cycle (in other words, region ABCDE).**
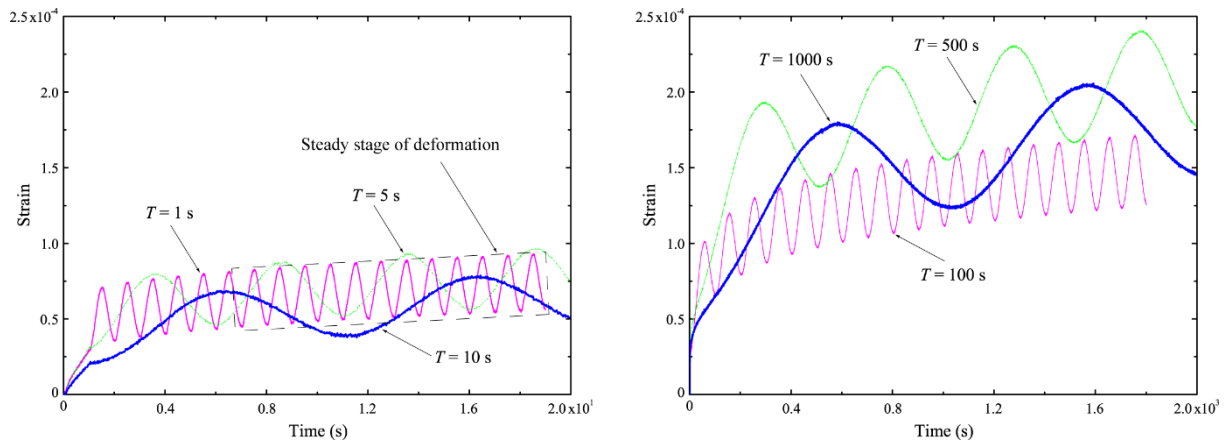
**Figure 8. Strain-time curves of specimen Dry-5ppt-1 tested with stresses varying from 0.08 to 0.25 MPa and with the temperature of -10°C.**
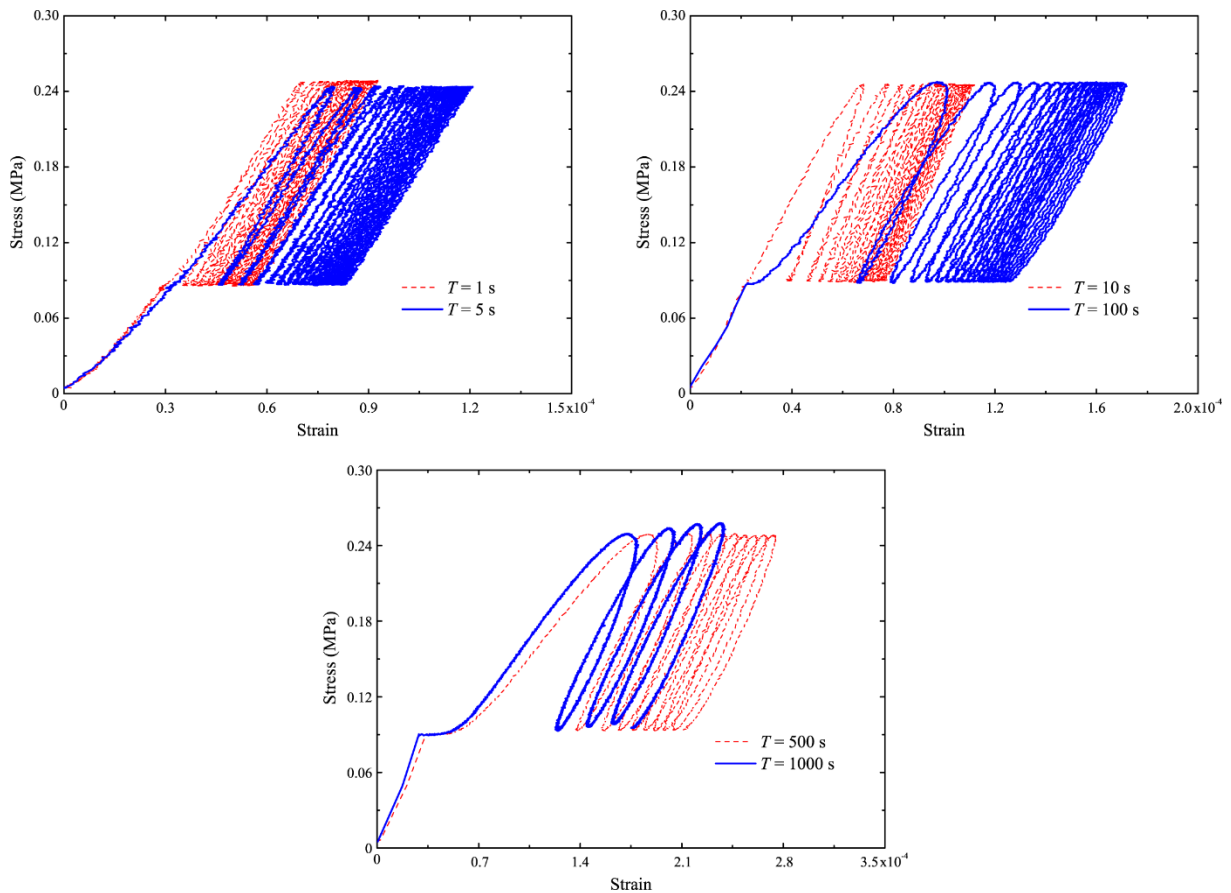
**Figure 9. Stress-strain curves of specimen Dry-5ppt-1 tested with stresses varying from 0.08 to 0.25 MPa and with the temperature of -10°C.**

645

(a)

(b)
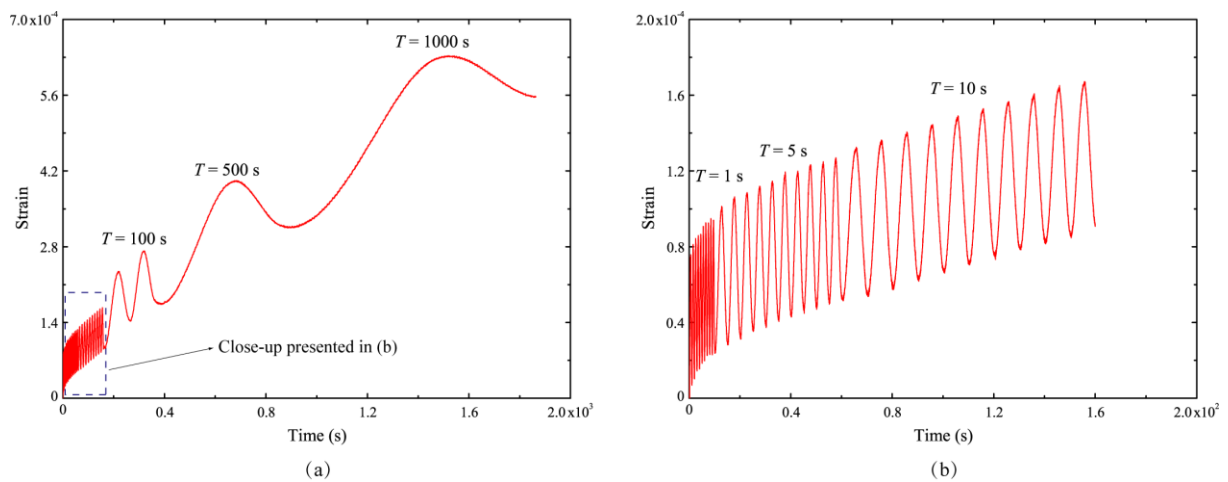
**Figure 10. Strain response of specimen Floating-5ppt-1 tested with stresses varying from 0.04 to 0.12 MPa and with the average temperature of -2.5°C: (a) shows the response for all periods, *T*, of cyclic loading, while (b) presents a close-up showing the cycles for *T* = 1, 5 and 10 s.**

(a)

(b)
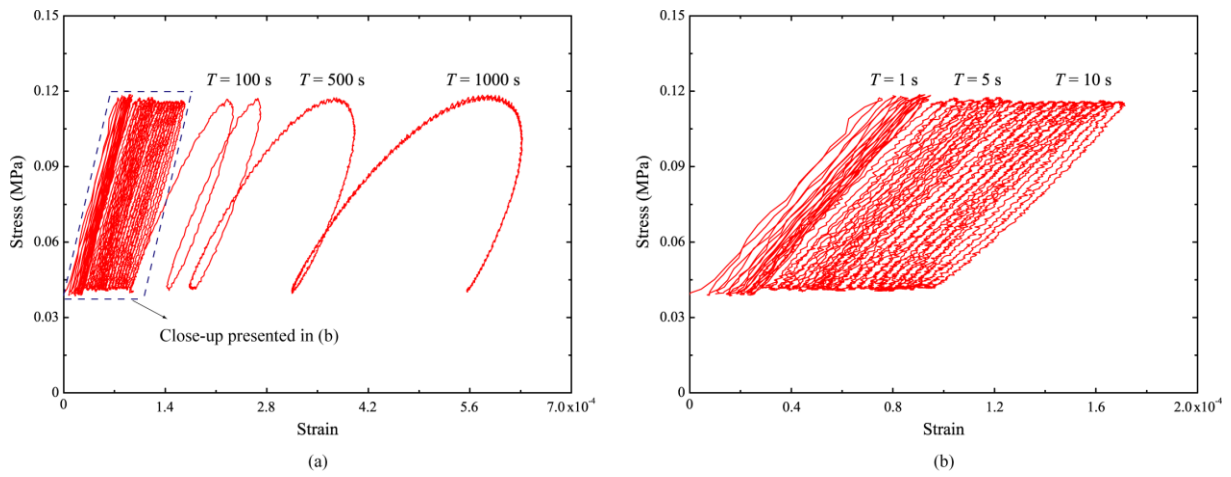
**Figure 11. Stress-strain plots of specimen Floating-5ppt-1 tested with stresses varying from 0.04 to 0.12 MPa and with the average temperature of -2.5°C: (a) shows the response for all periods, *T*, of cyclic loading, while (b) presents a close-up showing the cycles for *T* = 1, 5 and 10 s.**
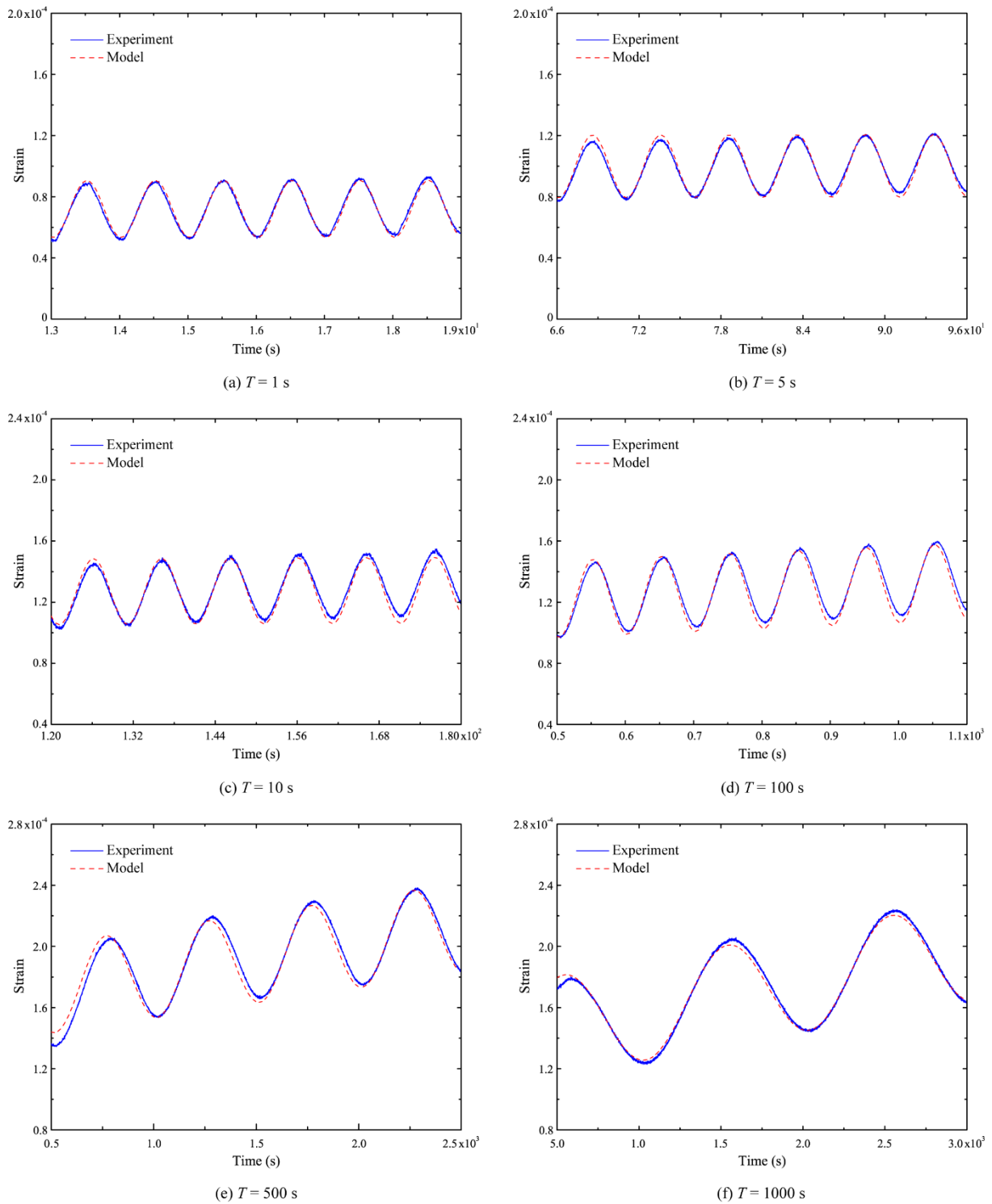
655

**Figure 12. Comparison between the experimentally measured strain-time curves (in the steady stage) and the results yielded by the physically based model for specimen Dry-5ppt-1 tested with stresses varying from 0.08 to 0.25 MPa and with the temperature of -10°C.**
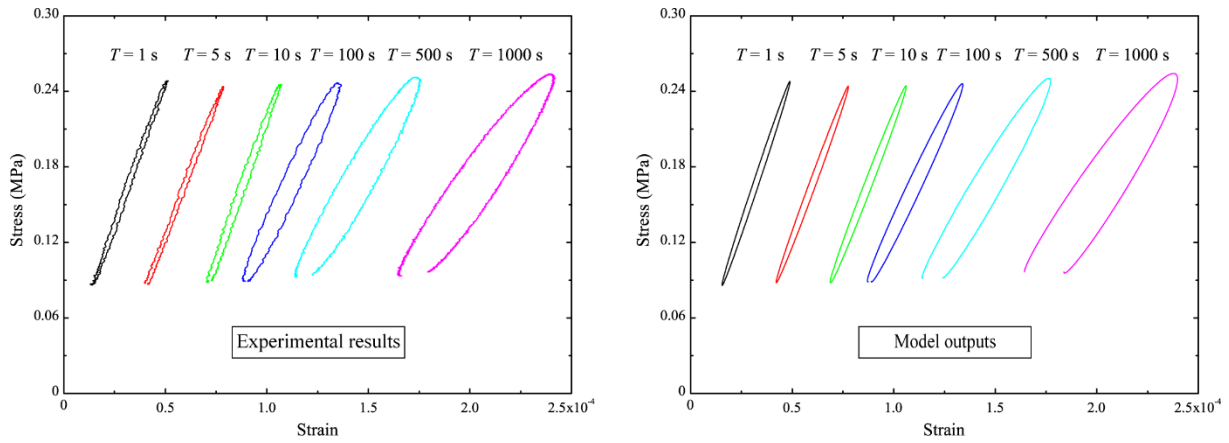
(a)
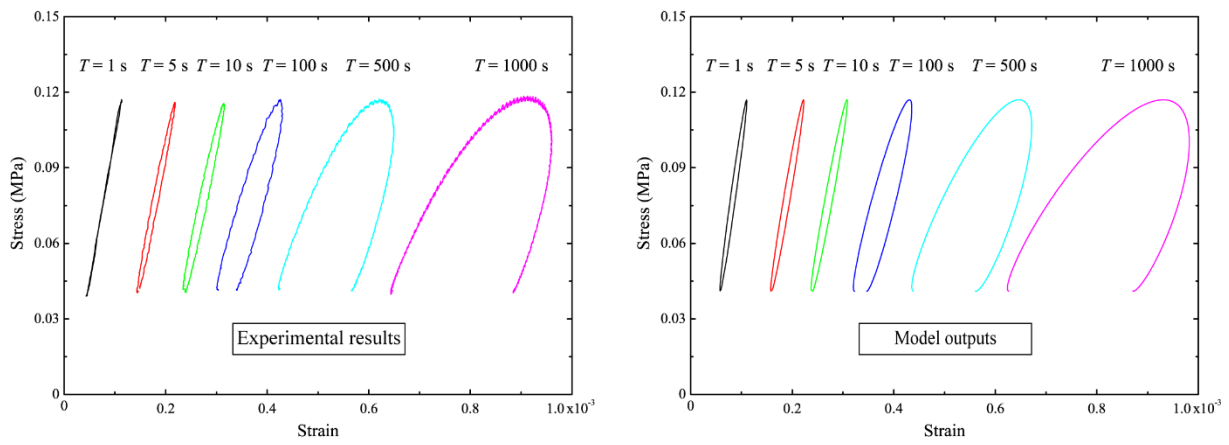
(b)

660

**Figure 13. Comparison between the steady-state stress-strain hysteresis loop measured in the experiments and that outputted from the model for (a) specimen Dry-5ppt-1 with the temperature of -10℃ and (b) specimen Floating-5ppt-1 with the average temperature of -2.5℃ (note that, to compare the representative hysteresis loops in all the different-frequency experiments with those outputted by the model in a more concise and intuitive way, the pre-strains before the hysteresis loops drawn here are not equal to the experimental values).**

665
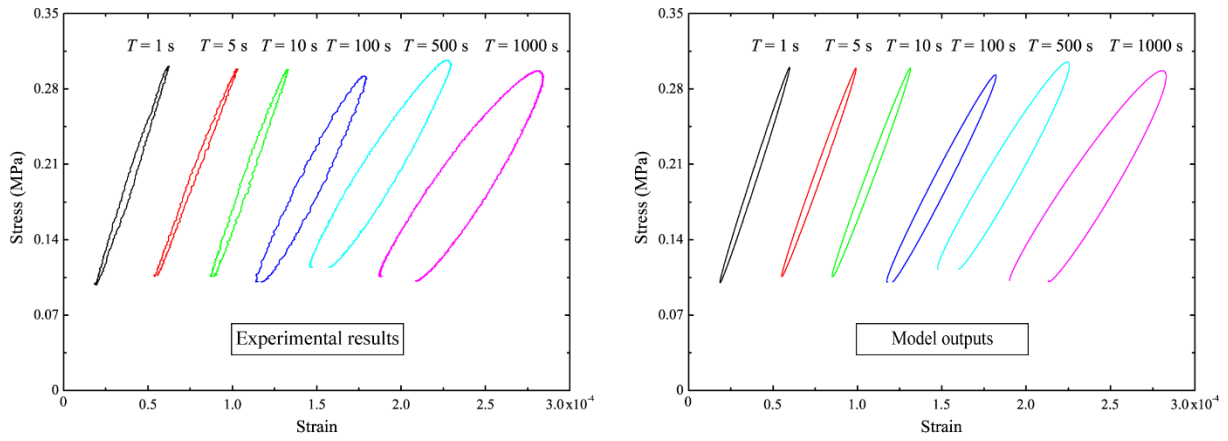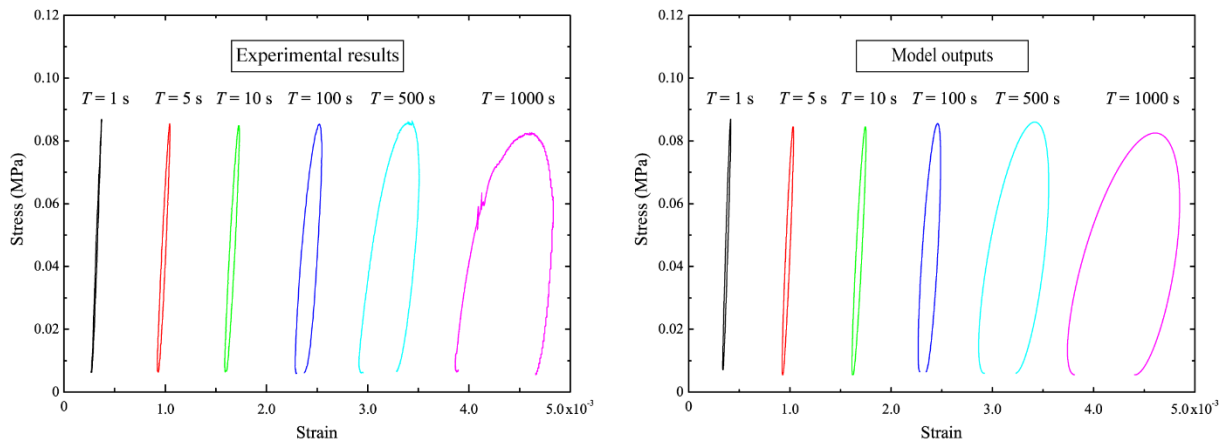
**Figure 14. Comparison between the steady-state stress-strain hysteresis loops measured in the experiments and those predicted by the dislocation-based model for (a) specimen Dry-5ppt-1 tested with stresses varying from 0.1 to 0.3 MPa and with the temperature of -10°C and (b) specimen Floating-5ppt-1 tested with stresses varying from 0.005 to 0.085 MPa and with the average temperature of -2.5°C (note that, to compare the representative hysteresis loops in all the different-frequency experiments with those outputted by the model in a more concise and intuitive way, the pre-strains before the hysteresis loops drawn here are not equal to the experimental values).**